Euro. Jnl of Applied Mathematics (2018), *vol.* 29, *pp.* 1062–1078.
doi:10.1017/S0956792518000074

Fragmentation of biofilm-seeded bacterial aggregates in shear flow†

E. P. KIGHTLEY[1,2], A. PEARSON[1,2], J. A. EVANS[3] and D. M. BORTZ[1]

[1]*Department of Applied Mathematics, University of Colorado, Boulder, CO 80309-0526, USA*
emails: Eric.Kightley@colorado.edu, Antony.Pearson@colorado.edu, dmbortz@colorado.edu
[2]*Interdisciplinary Quantitative Biology Graduate Program, University of Colorado, Boulder, CO 80309-596, USA*
[3]*Department of Aerospace Engineering Sciences, University of Colorado, Boulder, CO 80309-0429, USA*
email: john.a.evans@colorado.edu

(*Received 7 July 2017; revised 25 January 2018; accepted 25 January 2018; first published online 20 February 2018*)

We present a model for the force acting to fragment a biofilm-seeded microbial aggregate in shear flow, which we derive by coupling an existing model for the shape and orientation of a deforming ellipsoid with one for the surface force density on a solid ellipsoid. The model can be used to simulate the motion, shape, surface force density, and breakage of colloidal aggregates in shear flow. We apply the model to the case of exhaustive fragmentation of microbial aggregates in order to compute a post-fragmentation density function, indicating the likelihood of a fragmenting aggregate yielding daughter aggregates of a certain size.

Key words: 76Z99, 74F10, 92C10, 35Q92

1 Introduction

Fragmentation is an important dispersion strategy for bacterial biofilms, in which new colonies are eventually seeded from pieces of the original biofilm that have broken off. Once they are free-floating, such fragments can be treated as flocs. Microbial flocculation, the process whereby single-celled microbes in suspension persist as multicellular aggregates for a portion of their life-cycle, is ubiquitous in nature and industry, and considerable attention has, therefore, been devoted to modelling the dynamics of these systems [4,5,14, 18]. One popular approach is to solve some variation of a population-balance equation (PBE) for the size distribution of aggregates as a function of space and time [15,16]. Such models generally account for the fact that the microbial aggregates can break apart, for example, with the inclusion of a fragmentation kernel and post-fragmentation distribution in the population balance equation. Microbial aggregate fragmentation, however, remains a relatively poorly understood phenomenon. There exists a rich literature in rheology devoted to the study of fluid-fluid emulsions, and in particular to modelling the breakage and resulting size distributions of dispersed droplets (see [20], for a review), and for

† EPK is supported by the Interdisciplinary Quantitative Biology Program at the BioFrontiers Institute, University of Colorado Boulder (NSF IGERT 1144807) and by an NSF GRFP (DGE 1144083). This work was supported in part by grant NSF-DMS 1225878 to DMB.

this reason microbial aggregates are sometimes treated like ellipsoidal (hydrodynamically equivalent) droplets for the purposes of approximating their shape and motion [1,2,10,12, 13]. It is not clear, though, that the corresponding breakage and size-distribution models from the rheology literature on emulsions are equally applicable. The inhomogenous nature of microbial aggregates may mean that some breakage patterns are more likely than others, and we may wish to use knowledge about the structure and composition of the colloid, when modelling how and where they break.

This current work is a part of our long term efforts to develop a more accurate fragmentation model for use in PBE-based models. We have approached this problem using both *bottom-up* microscale modelling of individual flocs (this work and [6]) as well as a complementary *top-down* inverse problem methodology. The top-down approach takes time series of aggregate size-distributions and infers a post-fragmentation distribution [17] but does not incorporate any information about the heterogeneities in individual flocs. Here, we extend the bottom-up approach that we initially proposed in [6]. As described in [6], we have used confocal microscopy to identify three-dimensional (3D) positions of bacteria in a small number (39) of suspended aggregates. However, it is infeasible to experimentally obtain these types of 3D images for large populations of flocs. In [21], we used the 3D positions of bacteria in an aggregate to simulate the tumbling and deformation of bacterial flocs in laminar flow. However, it is also infeasible to perform large numbers of these simulations. Accordingly, we have pursued a hybrid approach merging models for the physics of viscous ellipsoids in flow with an analysis of the locations of high negative Gaussian curvature in the polysaccharides encapsulating the microbes.

Towards this end, we present a model to compute the force acting to break a microbial aggregate at a specified location. We call *aggregate fragmentation* the process in which a parent aggregate containing m microbes (its *size*) breaks into two *daughters* of sizes k and $m - k$. This is an extension of our earlier work in which we began to develop a framework for identifying likely breakage locations [6], and the present work expands upon this by introducing deformation to the model and by refining the computation of the fragmentation force. We construct our model by coupling a model for the deformation of a fluid droplet [9, 22] (hereafter, the *Deformation Constituent Model* or DCM) with one that computes the surface force density on a solid ellipsoid [3] (hereafter, the *Force Constituent Model* or FCM). We restrict ourselves to the case of viscous shear under the assumption of Stokes' flow, and our choice of deformation model is further guided by the requirements that (1) the surface remain ellipsoidal and (2) there be a restorative force (in this case interfacial tension) acting to oppose the deformation imposed by the shear field.

We then apply the model to the problem of generating a *post-fragmentation density function* $\Gamma(k \mid m)$, a conditional distribution giving the probability that an aggregate fragmentation event will yield a daughter aggregate of size k given that a parent of size m fragments. This density is often assumed to be normal or log-normal in the literature. The normal distribution is a model for the single event of an aggregate fragmenting into two (roughly) evenly-sized daughters. The log-normal distribution is a model for the cumulative effect of repeated fragmentation events (all with a normal post-fragmentation distribution) exhaustively until no more events are possible. We refer to these forms of fragmentation as *splitting*. In our previous work, we obtained a form of $\Gamma(k \mid m)$

https://doi.org/10.1017/S0956792518000074 Published online by Cambridge University Press

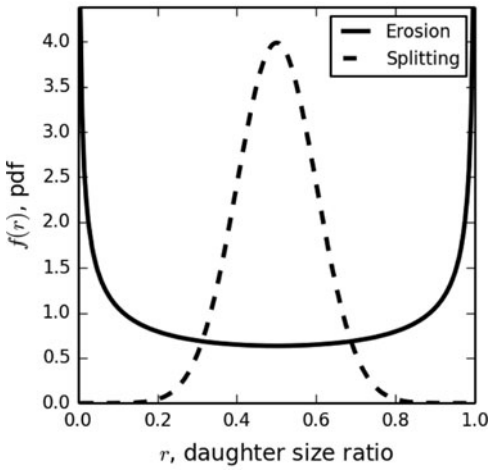

FIGURE 1. Example post-fragmentation density functions corresponding to erosion and splitting fragmentation mechanisms.

corresponding to fragmentations yielding one daughter much larger than the other, which we refer to as *erosion* [6]. Example distributions following each of these fragmentation mechanisms can be seen in Figure 1. In our previous simulations, we found that larger aggregates tended to fragment by erosion, whereas smaller ones tended to fragment by splitting. Here, we reproduce and expand upon these simulations with the improved fragmentation force model.

The paper is organised as follows. In Section 2, we present the methods: first describing the DCM and FCM constituent models and how we couple them (Section 2.1), then using the coupled models to define the concept of fragmentation force (Section 2.2), and last explaining how we apply this concept to microbial aggregate fragmentation (Section 2.3). In Section 3, we present the results of our simulations, beginning with an exploration of the motion and orientation of an aggregate under the DCM (Section 3.1), followed by a discussion of the fragmentation force (Section 3.2), and the application of this model to microbial aggregate fragmentation and the generation of post-fragmentation density functions (Section 3.3). We finish with some concluding remarks as well as a brief outline of our plans for upscaling these results for use in a PBE equation (Section 4).

2 Methods

2.1 Constituent models

Deformation constituent model (DCM)

The DCM is the model, which we use to describe the deformation and rotation motion of a fluid ellipsoid in simple shear flow. This model is developed in [9, 22], to which the reader is referred for a full development. Here, we present only the material necessary for the coupling of the models. An arbitrary ellipsoid centred at the origin can be represented by a shape tensor, a symmetric 3×3 tensor $\mathbf{G}$ such that $\mathbf{x}^T\mathbf{G}\mathbf{x} = 1$ for any point $\mathbf{x}$ on

https://doi.org/10.1017/S0956792518000074 Published online by Cambridge University Press

the surface of the ellipsoid. The shape tensor is orthogonally diagonalisable, so that

$$\mathbf{D} = \mathbf{R}^T \mathbf{G} \mathbf{R}, \tag{2.1}$$

where $\mathbf{D}$ is diagonal and $\mathbf{R}$ is a rotation. We can choose to construct $\mathbf{G}$ such that the diagonal entries of $\mathbf{D}$ (the eigenvalues of $\mathbf{G}$) λ_i are defined by $\lambda_i = 1/a_i^2$, where $\mathbf{a} = (a_1, a_2, a_3)$ are the axes lengths of the ellipsoid.

The DCM consists of an ODE we can solve for such a shape tensor $\mathbf{G}(t)$. Assuming constant volume and Stokes flow in an incompressible Newtonian fluid, the governing equation for shape of the ellipsoid is

$$\dot{\mathbf{G}} + \mathbf{L}_d^{\mathrm{T}} \cdot \mathbf{G} + \mathbf{G} \cdot \mathbf{L}_d = 0, \tag{2.2}$$

where $\mathbf{G}$ is the shape tensor of the ellipsoid, as described above, $\dot{\mathbf{G}}$ is the material derivative of $\mathbf{G}$, and $\mathbf{L}_d$ is the droplet velocity gradient.

To solve equation (2.2) for $\mathbf{G}$, an expression for $\mathbf{L}_d$ is required; this expression must depend only on the external velocity gradient $\mathbf{L}$, the shape and orientation of the ellipsoid, and the input parameters. The reader is referred to [9, 22] for derivations and the precise form of $\mathbf{L}_d$. For our purposes, it suffices to note that the output of solving the DCM will be a time-series of shape tensors $\mathbf{G}(t_i)$ satisfying equation (2.2).

Force Constituent Model (FCM)

Here, we describe the FCM developed in [3]. Given an ellipsoid with axes lengths a_i such that $a_1 \geqslant a_2 \geqslant a_3$, under the assumption of Stokes' flow, the force density on the surface of a solid ellipsoid in simple shear can be written as

$$\mathbf{f} = \left(-p_0 \mathbf{I} - 4\mu \sum_{j=0}^{3} \chi_j A_j^j \mathbf{I} + \frac{8\mu}{a_1 a_2 a_3} \mathbf{A}^T \right) \mathbf{n}, \tag{2.3}$$

where p_0 is the external pressure, μ is the matrix viscosity, a_i are the axes lengths, and $\mathbf{n}$ is normal to the surface of the ellipsoid. The matrix $\mathbf{A}$ is in turn defined by

$$A_k^i = \begin{cases} \dfrac{3\chi_i'' E_i^i - \sum_{l=1}^{3} \chi_l'' E_l^l}{6(\chi_1'' \chi_2'' + \chi_1'' \chi_3'' + \chi_2'' \chi_3'')} & \text{for } i = k, \\ \dfrac{\chi_i E_k^i + a_k^2 \sum_{l=1}^{3} \varepsilon^{ikl} \chi_l' (\varepsilon^{ikl} \Omega_k^i + \omega_l)}{2(a_k^2 \chi_k + a_i^2 \chi_i) \sum_{l=1}^{3} |\varepsilon^{ikl}| \chi_l'} & \text{for } i \neq k, \end{cases} \tag{2.4}$$

where $\mathbf{E} = \frac{1}{2}(\mathbf{L} + \mathbf{L}^{\mathrm{T}})$ is the rate-of-strain tensor, $\boldsymbol{\Omega} = \frac{1}{2}(\mathbf{L} - \mathbf{L}^{\mathrm{T}})$ is the vorticity tensor, and ω_l is the lth component of the angular velocity $\boldsymbol{\omega}$ of the ellipsoid. The elliptic integrals χ_j used are defined by

$$\chi_j = \int_0^{\infty} \frac{d\xi}{(a_j^2 + \xi)\sqrt{(a_1^2 + \xi)(a_2^2 + \xi)(a_3^2 + \xi)}}, \tag{2.5}$$

https://doi.org/10.1017/S0956792518000074 Published online by Cambridge University Press

with

$$\chi_i^{'} = \frac{\sum_{k,l=1}^{3} \varepsilon^{ikl}(\chi_l - \chi_k)}{\sum_{k,l=1}^{3} \varepsilon^{ikl}(a_k^2 - a_l^2)} \tag{2.6}$$

and

$$\chi_i^{''} = \frac{\sum_{k,l=1}^{3a} \varepsilon^{ikl}(a_k^2\chi_k - a_l^2\chi_l)}{\sum_{k,l=1}^{3} \varepsilon^{ikl}(a_k^2 - a_l^2)}. \tag{2.7}$$

Coupling the constituent models

The matrix $\mathbf{A}$ in equation (2.4) depends upon the matrix velocity gradient $\mathbf{L}$ and the angular velocity $\boldsymbol{\omega}$ of the ellipsoid, both of which must be expressed in a frame of reference relative to the centre of the ellipsoid; i.e., one that rotates with respect to the external frame of reference. In the case of a solid ellipsoid in shear flow, there are analytic representations for both of these quantities [3], but in our model, the motion of the ellipsoid is dictated by the DCM, and we must therefore compute $\mathbf{L}$ and $\boldsymbol{\omega}$ numerically as they do not have closed-form solutions. The rotation connecting the two reference frames is represented by the matrix $\mathbf{R}(t)$ in equation (2.1), which we obtain by diagonalising the solution $\mathbf{G}(t)$ to the DCM, equation (2.2). In simple shear flow, the velocity gradient $\mathbf{L}$ is constant in time in an external frame of reference. If the ellipsoid rotates according to $\mathbf{R}(t)$ in the external frame, then the shear field rotates according to $\mathbf{R}^T(t)$ in the ellipsoid frame. Thus, we set $\mathbf{L}_R(t) = \mathbf{R}(t)\mathbf{L}\mathbf{R}^T(t)$, and use $\mathbf{L}_R$ in equation (2.3). Expressing the angular velocity in the anti-symmetric matrix

$$[\boldsymbol{\omega}(t)]_\times \equiv \begin{pmatrix} 0 & -\omega_z & \omega_y \\ \omega_z & 0 & -\omega_x \\ -\omega_y & \omega_x & 0 \end{pmatrix}, \tag{2.8}$$

a straightforward calculation tracking the motion of an arbitrary point on the ellipsoid surface yields the relation

$$[\boldsymbol{\omega}(t)]_\times = \left(\mathbf{R}(t)\mathbf{R}'(t)\right)^T. \tag{2.9}$$

We approximate $\mathbf{R}'(t)$ using the discretised solution $\mathbf{R}(t_i)$ to equation (2.2), and then use equation (2.9) to compute $[\boldsymbol{\omega}(t)]_\times$, giving $\boldsymbol{\omega}$, the angular velocity of the ellipsoid in the external frame. In the ellipsoid frame, the shear field is rotating in the opposite direction, with angular velocity $-\boldsymbol{\omega}$. This is the quantity we use in equation (2.3).

2.2 Fragmentation force

In this section, we develop the concept of the fragmentation force, an approximation to the force acting to pull apart a deformable ellipsoidal particle in shear flow. To do so, we will use the coupled models described in the preceding section to compute an integral of the force density on the surface of the ellipsoid. We define the fragmentation force in such a manner as to permit us to specify where we think breakage will occur by way of a *fragmentation plane*, $\mathcal{P}$, which intersects the ellipsoid. We introduced a similar concept in our previous work [6] for use on non-deformable ellipsoidal approximations to

https://doi.org/10.1017/S0956792518000074 Published online by Cambridge University Press

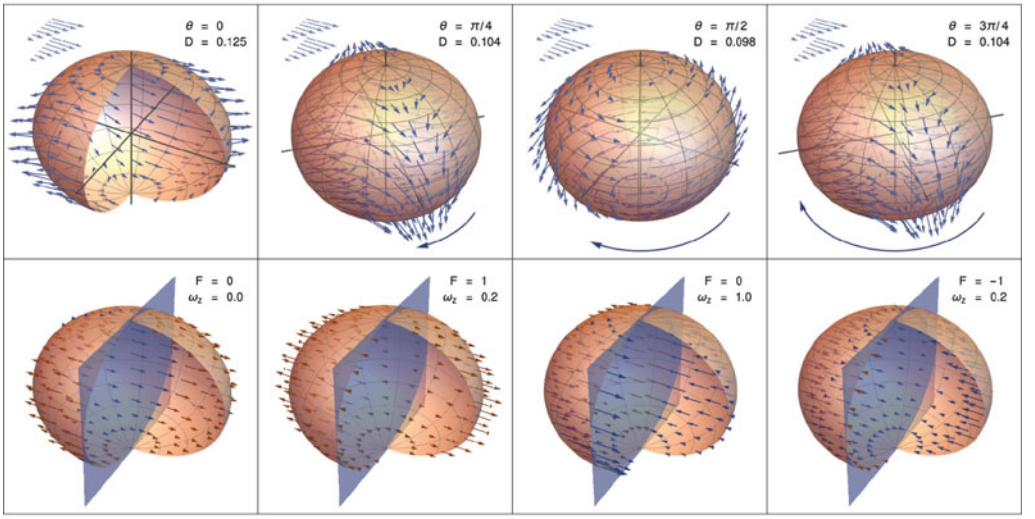

FIGURE 2. A sample ellipsoid shown at four characteristic time points. The ellipsoid is undergoing periodic tumbling with mild deformation. First row: view from an external reference frame, with surface forces and flow field. $D = (a_1 - a_3)/(a_1 + a_3)$ is the Taylor deformation parameter, θ is the angle through which the ellipsoid has rotated. Second row: view from the ellipsoid reference frame, with components of the surface force acting to push into (blue) and pull against (red) a sample fragmentation plane. F is the relative fragmentation force with respect to the plane, and ω_z is the relative angular velocity.

microbial aggregates. In practice, the location and orientation of $\mathcal{P}$ is to be chosen based upon structural information about the aggregate. In our aforementioned application, for example, we preferentially chose planes corresponding to locations where we expected the surface of the microbial aggregate to exhibit a more negative Gaussian curvature.

Suppose that we have chosen some plane $\mathcal{P}$ defined by a normal vector $\mathbf{n}_p$ and interior point $\mathbf{x}_p$, so that $\mathbf{n}_p \cdot (\mathbf{x}_p - \mathbf{x}) = 0$. Let $\mathbf{f}(\mathbf{x})$ be the force density at point $\mathbf{x}$ on the surface $\mathcal{E}(t)$ to an ellipsoid at time t, computed from equation (2.3) as described the preceding section. Define the fragmentation force as defined as

$$F = \int_{\mathcal{E}(t)} s(\mathbf{x}, P)\, |\mathbf{f}(\mathbf{x}) \cdot \mathbf{n}_p|\, d\mathbf{x}, \tag{2.10}$$

where

$$s(\mathbf{x}, P) = \begin{cases} 1 & \text{if } \mathbf{f}(\mathbf{x}) \text{ acts to pull against } P \\ -1 & \text{if } \mathbf{f}(\mathbf{x}) \text{ acts to push into } P \end{cases}. \tag{2.11}$$

The integrand is, thus, the signed magnitude of the component of $\mathbf{f}$ acting against $\mathcal{P}$, where s indicates whether this component acts to pull against or push into the plane. Thus, s explicitly accounts for the fact that some of the surface force density may in fact compress against the plane and thus oppose breakage. Figure 2 shows snapshots of an ellipsoid in flow along with sample force density vectors, as well as with a sample fragmentation plane and components of the surface force density acting normal to it. As

https://doi.org/10.1017/S0956792518000074 Published online by Cambridge University Press

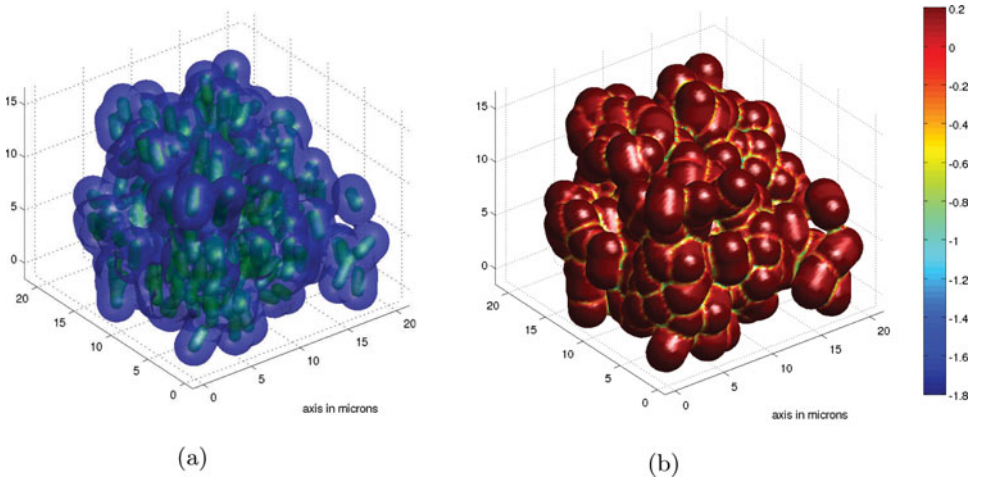

(a) (b)

FIGURE 3. Two illustrations of a bacterial aggregate in the dataset described in [6]. There are 253 bacteria in this aggregate. (a) Bacterial aggregate reconstructed from confocal microscopy slices. Green surface is the cell wall. Blue surface is the approximate edge of the extracellular polymeric substance (EPS) surface. (b) Same bacterial aggregate as in Figure 3(a). Colours correspond to the Gaussian curvature computed on the EPS surface. The regions with the most negative curvature are energetically unfavourable and are the best candidates for separation.

can be seen in the second row of the figure, sometimes the force density acts to compress against the plane (blue arrows) and sometimes to pull against it (red arrows).

2.3 Aggregate fragmentation

Having defined the fragmentation force, we now wish to apply it to the case of aggregate fragmentation. To do so, we begin with a dataset indicating the coordinates of bacterial centres of mass in 39 *Klebsiella pneumoniae* aggregates (dataset described in [6]). Depicted in Figure 3 are two visualisations of a 3D reconstruction of one of the bacterial aggregates. In Figure 3(a), the green surface is the *Klebsiella pneumoniae* cell wall and the blue surface is an estimated location of the edge of the extracellular polymeric substance (EPS) surrounding the bacteria (1 micron away from the cell wall). Practically speaking, the edge of the EPS is not well-defined and as described in [7], the density of the EPS is highest near the wall and decays within a few microns of the wall. In Figure 3(b), the same floc is shown with the Gaussian curvature (K) computed on the approximate EPS surface. The regions with large negative K are energetically unfavourable for soft matter [11], and are thus the best candidates for potential breakage.

To compute the forces on a tumbling and deforming aggregate is non-trivial[1]. We choose to approximate the forces on the aggregate surface with the forces on a hydrodynamically equivalent ellipsoid. Thus, the first task is to approximate an aggregate's surface with an ellipsoid, which can then rotate and deform over time according to the DCM, equation

[1] See [8, 21] for illustrations of the challenges of simulating the biomechanics of communities of bacteria.

https://doi.org/10.1017/S0956792518000074 Published online by Cambridge University Press

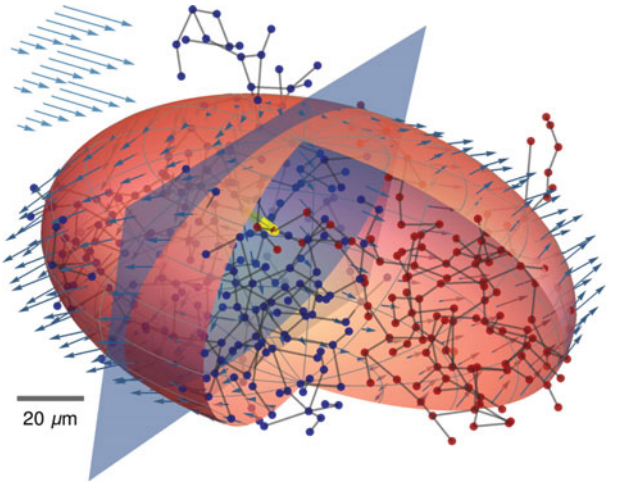

FIGURE 4. Mathematical representation of an aggregate. Bacterial centres of mass (blue and red points) are connected by a minimum spanning tree and sample force density vectors are shown on the ellipsoidal surface. An intersecting plane bisects the (yellow) highlighted edge of the MST. The centres of mass are colour-coded (red and blue) to indicate the two daughter aggregates that would result from a fragmentation at this edge.

(2.2). At any particular time point, we further wish to specify a fragmentation plane $\mathcal{P}$ based on some structural property of the aggregate, and then use equation (2.10) to compute the force acting to break the aggregate along $\mathcal{P}$. If the force is large enough, the aggregate will fragment into two daughters. We proceed to describe the details of this process. Figure 4 shows the various constructs derived below.

Ellipsoidal representation

In order to apply the model we have developed above, we must represent the surface of an aggregate as a hydrodynamically equivalent ellipsoid. The justification for this process is detailed in [6]. Beginning with the coordinates of an aggregate's bacterial centres of mass, we first translate them so they are centred about the origin. We then rotate the coordinates using a principal components decomposition so that the maximal variation lies along the x-axis, then the y-axis, and finally the z-axis of the coordinate system. We take an ellipsoid with axes lengths equal to twice the standard deviation along each axis. The ellipsoid axes lengths specify the initial shape tensor $\mathbf{G}_0$ for the governing equation (2.2), and given the remaining parameters we can then solve this equation to obtain the shape and orientation of the ellipsoid over time, which is fully specified by the axes lengths $\mathbf{a}(t)$ and a rotation $\mathbf{R}(t)$.

Location of fragmentation plane

In order to check for fragmentation, we must specify the intersecting plane used to compute the force in equation (2.10). To rapidly identify candidate breakage locations, we will create a spanning tree connecting the bacterial centres of mass. If we let $\mathcal{M}$ be

https://doi.org/10.1017/S0956792518000074 Published online by Cambridge University Press

a *minimum spanning tree* (MST), then longer edges in the tree will coincide with regions of the most negative Gaussian curvature. As any fragmentation of the aggregate must sever at least one edge of $\mathcal{M}$, we choose these edges as potential fragmentation locations. Given an edge e of $\mathcal{M}$, we define the plane $\mathcal{P}_e$ that bisects e and is normal to it. Thus, $\mathcal{P}_e$ is normal to $\mathbf{x} - \mathbf{y}$ and passes through $\frac{1}{2}(\mathbf{x} - \mathbf{y})$, where $\mathbf{x}$ and $\mathbf{y}$ are the coordinates of the nodes of e. Supposing that we have chosen an edge e, then at any time point t we can compute the fragmentation force using equation (2.10), which we now denote as $F(e, t)$.

This procedure is illustrated in Figure 4. The red and blue dots are the centres of mass of each bacteria in the aggregate, and the grey lines are the edges of a MST connecting them. The highlighted edge near the centre of the aggregate is an example candidate edge for fragmentation. The blue plane is the fragmentation plane that bisects this edge and is normal to it. The bacterial centres of mass are then colour-coded according to which side of the MST they belong to, so that if the aggregate were to fragment at this edge, the red centres of mass would form one daughter aggregate and the blue centres of mass would form the other daughter.

Fragmentation of an aggregate

If the force $F(e, t)$ exceeds some threshold f_{crit}, then the aggregate will fragment. We remove the edge e from the MST $\mathcal{M}$, which will result in two new trees. Each tree will become a new aggregate, which we construct by rotating and scaling the original bacterial centres of mass according to the shape and orientation of the ellipsoid $\mathcal{E}$ at time t. If $\mathbf{x}(0)$ are the coordinates of a bacterial centre of mass at time $t = 0$, $\mathbf{R}(t)$ is the rotation specifying the orientation of $\mathcal{E}(t)$, and $\mathbf{a}(t)$ are the axes lengths of the ellipsoid, then the location of the centre of mass at time t is

$$\mathbf{x}(t) = \mathbf{R}(t) \cdot \frac{\mathbf{a}(t)}{\mathbf{a}(0)},$$

where the division is taken element-wise. In this manner, we can transform the centres of mass in each of the two new aggregates.

We have not yet specified how we wish to choose the edge e. Ultimately, we will check all of the edges, but the order in which we do so matters. We use three different methods for comparison. In our simulations, the ellipsoid shape and orientation is cyclic in time, and hence it suffices to compute the fragmentation force over a single period T. Suppose the edges in the MST are sorted by their lengths at time $t = 0$. The *first edge* method gives the longest edge in the MST the chance to break before checking any other edges, so that if at some time t in T we find that $F(e_1, t) > f_{\text{crit}}$, then the aggregate fragments at e_1 at time t. Should $F(e_1, s)$ never exceed f_{crit}, then we check e_2 at all time points, and so on. This is the method we employed in our previous work [6], arguing that longer edges ought to be associated with surface regions possessing large negative Gaussian curvature, which in turn would thus be more likely to break. The next method, *first time*, still gives preferential treatment to longer edges, but checks the force on each edge at time s before moving on to time $s + \Delta t$, so that a shorter edge e_j $(j > 1)$ has the opportunity to break at time s before any edge at time $s + \Delta t$. Last, the *global maximum* method computes $F(e, t)$ for all edges and all times in the discretisation, and chooses the largest one, $F_{\max}$, which

https://doi.org/10.1017/S0956792518000074 Published online by Cambridge University Press

Table 1. *Model parameters*

Symbol	Parameter	Model	Range	Units
$\mathbf{a}(t)$	Axes lengths	D, F	$1–1{,}000\times10^{-6}$	m
$\boldsymbol{\omega}(t)$	Angular velocity	F	0–100	1/s
$\mathbf{L}(t)$	Velocity gradient	D, F	0–10	1/s
μ	Matrix viscosity	D, F	8.95×10^{-4}	Pa s
λ	Viscosity ratio	D	1–100	–
Γ	Interfacial tension	D	$10^{-9} - 10^{-7}$	N/m

occurs at some edge d and time t. If $F_{\max} > f_{\text{crit}}$, then the aggregate fragments along edge d and at time t. This method gives no preferential treatment to either time or edge length.

Post-fragmentation density function

Given an aggregate and a fragmentation method, we can check for fragmentation as described above. If the aggregate fragments, we then have two new aggregates that we can submit to the same procedure. Eventually fragmentation will stop, either because all of the aggregates are reduced to singletons, which cannot fragment, or because all remaining aggregates experience a maximum fragmentation force below the critical force f_{crit}. We refer to this process as *exhaustive fragmentation*. Keeping track of the sizes of all intermediate flocs, we can then compute the density of fragmentations by the size of the parent aggregate. This in turn permits the construction of a post-fragmentation density function $\Gamma(k \mid m)$, which gives the probability of a fragmentation resulting in daughters of size k and $m - k$ given that an aggregate of size m fragments. We will construct $\Gamma(k \mid m)$ for each of the three fragmentation methods described above.

Model parameters

The model parameters are described in Table 1. The DCM depends upon the initial axes lengths a_i of the ellipsoid, the velocity gradient $\mathbf{L}$, the matrix viscosity μ, the viscosity ratio λ, which is the ratio of the droplet viscosity over the matrix viscosity, and the interfacial tension Γ. The FCM depends upon the axes lengths $a_i(t)$ at each time point, the angular velocity of the ellipsoid $\boldsymbol{\omega}(t)$, and the velocity gradient $\mathbf{L}(t)$, which now also has a dependence on time due to the rotating frame of reference. In all of our simulations, we set the external pressure p_0 to 0. Under this parameter regime, taking the external (matrix) fluid to be water, the Reynolds number is typically of order 10^{-2}, although adversarial choices of the length scale and velocity can give a Reynolds number of order 1. Reducing the shear rate by an order of magnitude results in very little deformation of the ellipsoids, which effectively reproduces our earlier simulations of the fragmentation of solid ellipsoids. We use $\dot{\gamma} \sim 1\text{s}^{-1}$ to enforce some deformation, even though this increases the Reynolds number beyond a desirable order for Stokes' flow simulations.

We must make a further cautionary remark regarding the interpretability of the parameter values in our model. The viscosity ratio and interfacial tension parameters serve to induce a particular behaviour in the system (oscillating deformation with tumbling,

https://doi.org/10.1017/S0956792518000074 Published online by Cambridge University Press

as we will discuss below), but the mechanisms physically responsible for this behaviour are more likely viscoelastic. There are attractive and repulsive forces between the cells in the aggregates, for example, and the cohesion and retraction of the ellipsoidal shape is surely due to these rather than interfacial tension. We will later observe the qualitative dependence of our model's behaviour on its parameters, and in so doing we must be careful not to overstate the physical interpretability of the specific values these parameters take. Their ranges were chosen to induce the oscillating behaviour we expect to see, and should not be taken as representative of a physical regime of interest.

3 Results

3.1 Motion under the DCM

Characteristic behaviours of the DCM

An ellipsoid evolving according to the DCM follows one of three characteristic behaviours: it can (1) collapse smoothly to a steady-state orientation and shape (Figure 5(a)), (2) collapse while oscillating to a steady-state orientation (Figure 5(b)), or (3) oscillate periodically (Figure 5(c)). The angular velocity of the oscillating collapse (Figure 5(b)) can often exhibit a sudden 'flip' in which the direction of rotation of the ellipsoid changes. This occurs when two of the axes lengths are close in magnitude. In the remainder of the present work, we restrict ourselves to the case of periodic tumbling (see Figure 5(c)), which we believe to be the most physically accurate for the case of microbial aggregates.

Futhermore, we expect it is unphysical for such an aggregate to become too elongated, and even if it were to, there is no reason to expect under such a circumstance that the model we employ here would accurately capture the physics responsible for such deformation. In such circumstances, we might instead turn to a viscoelastic model of suspended colloids, such as in [19]. We therefore wish to restrict the maximum magnitude of axes length oscillations, which we can characterise with the parameter $d_{\max} = \max a_1(t)/\min a_1(t)$. The magnitude of the axes length oscillations depends primarily on the viscosity ratio and the shear rate, and we observe in practice that the other restrictions we impose on these parameters (Table 1) result in bounding $d_{\max} < 2$.

Limiting viscosity

In the oscillatory regime shown in Figure 5(c), the behaviour of the deforming ellipsoid approaches that of a solid ellipsoid. In simple shear defined by $d\mathbf{u}/dy = \dot{\gamma}$, the angle $\theta(t)$ in the xy plane of a solid ellipsoid is given ([23] c.f. [3]) by

$$\theta_{solid}(t) = -\arctan\frac{a_1}{a_2}\tan\left(\frac{2\pi t}{T}\right), \tag{3.1}$$

where

$$T = \frac{2\pi(a_1^2 + a_2^2)}{a_1 a_2 \dot{\gamma}}, \tag{3.2}$$

https://doi.org/10.1017/S0956792518000074 Published online by Cambridge University Press

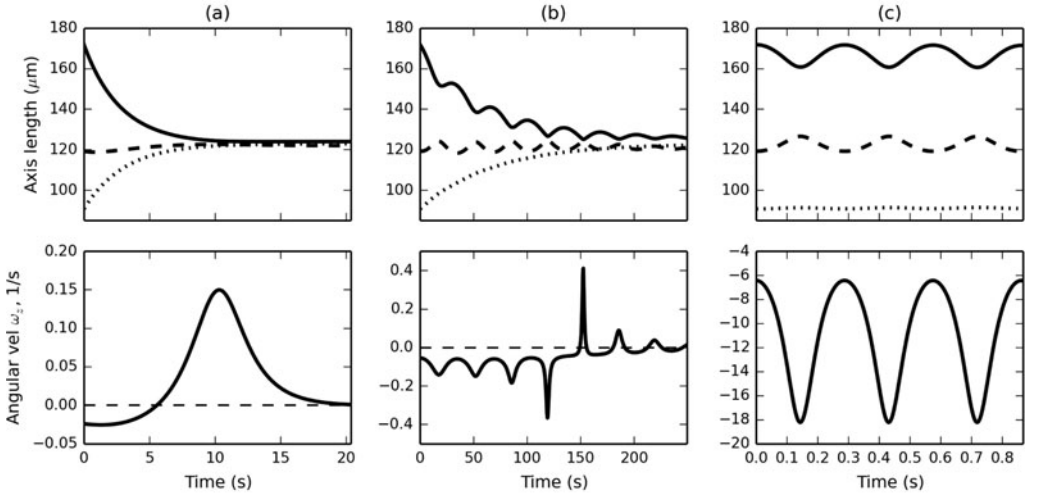

FIGURE 5. Characteristic behaviours of ellipsoids evolving in the DCM: (a) collapse (Ca $\sim$ .294), (b) oscillating collapse (Ca $\sim$ 13.2), and (c) periodic tumbling (Ca $\sim$ 3441). Here, Ca is the capillary number, defined by $\mathrm{Ca} = \mu V/\Gamma$, where μ is the dynamic viscosity of water, $V \sim \|\mathbf{a}\|\dot{\gamma}$ is a characteristic velocity, and Γ is the interfacial tension.

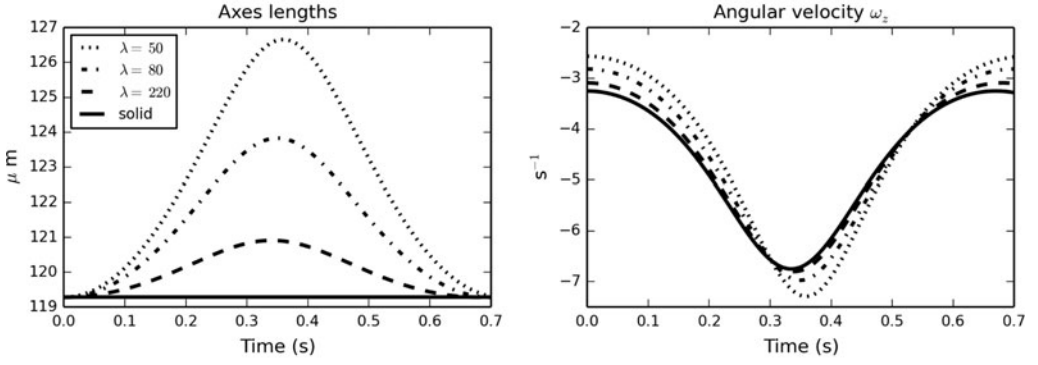

FIGURE 6. Asymptotic behaviour of the DCM as $\lambda \to \infty$ (dashed lines) compared to the behaviour of a solid ellipsoid with angular velocity given by equation (3.3) (solid line). Left: second axis length (a_2) over time, right: angular velocity component ω_z over time.

is the period of the rotation. From this, we can compute the angular velocity component ω_z as

$$\omega_{z,solid} = -\frac{2\pi}{T}\frac{a_1 a_2 \sec^2\left(2\pi t/T\right)}{a_2^2 + a_1^2 \tan^2\left(2\pi t/T\right)}. \tag{3.3}$$

In the limit $\lambda \to \infty$, a fluid droplet becomes a solid, in which case we expect that the axes lengths will become constant and the angular velocity computed using equation (2.9) will approach that given in equation (3.3). This is indeed what we observe; as the viscosity ratio increases, the axis length oscillations decrease (Figure 6(a)) and the angular velocity converges to that of a solid ellipsoid (Figure 6(b)).

https://doi.org/10.1017/S0956792518000074 Published online by Cambridge University Press

3.2 Fragmentation force

Qualitative behaviour

Figure 2 shows the evolution in time of a generic ellipsoid at four time-points, including the surface force density as well as the component of this density acting normal to a sample fragmentation plane. This ellipsoid is undergoing periodic tumbling, as in Figure 5(c), with mild deformation. In the first frame, at the initial time, we observe that the surface force density points both outwards and inwards. This feature is responsible for the fact that at the third time-point, when the angular velocity is maximised which in turn causes the surface force density magnitudes to be maximised, we nevertheless observe a net fragmentation force of 0. The maximum fragmentation force is observed at the second time-point, when all of the force vectors act against the plane, and the minimum, which is negative, occurs at the fourth time-point, when all of the surface force vectors push into the plane.

Parameter dependence

Intersecting a generic ellipsoid $\mathcal{E}$ with a plane P defined by the normal $\mathbf{n}_p = (1, 0, 0)$ and interior point $\mathbf{x}_p = (0, 0, 0)$, i.e., a plane in the yz plane passing through the origin and normal to the longest major axis of $\mathcal{E}$. We first explore the dependence of the fragmentation force, equation (2.10), on the system parameters. We compute the maximum fragmentation force as a function of the shear rate $\dot{\gamma}$, the viscosity ratio λ (which we vary while holding the matrix viscosity μ constant, changing only μ^*), and the interfacial tension Γ. As can be seen in Figure 7(a), the fragmentation force increases with the shear rate. The shear rate appears directly in the computation of the surface force density in equation (2.3), and indirectly as it affects the angular velocity $\boldsymbol{\omega}$. At higher shear rates, there is a greater dependence of $f_{\max}$ on the viscosity ratio, and its dependence on λ is non-linear, changing more for smaller values of λ while being constant at higher values of λ. The dependence of $f_{\max}$ on Γ and λ is shown in Figure 7(b). Again, $f_{\max}$ increases with λ; in addition, it can be seen to decrease with Γ. Neither of these terms appear directly in the force equation (2.3), and so their influence on $f_{\max}$ manifests through their role in shaping the motion and deformation of the ellipsoid as in equation (2.2).

Maximising fragmentation force as a function of plane location

We next consider the fragmentation force as a function of time and position of the intersecting plane. We construct the ellipsoid as above, except that now we will slide the intersecting plane along the x-axis. These results are shown in Figure 8. The x-axis corresponds to the position of the interior point on the intersecting plane, so that at a point x on this axis, the intersecting plane is defined by normal $\mathbf{n}_p = (1, 0, 0)$ and $\mathbf{x}_p = (x, 0, 0)$. The y-axis corresponds to time. The fragmentation force is anti-symmetric about its horizontal centre, which corresponds to the point in time at which the ellipsoid has rotated through an angle of $\pi/2$. Past this point, the symmetry of the system results in the surface forces being equal in magnitude but opposite in sign. As the plane slides along the

https://doi.org/10.1017/S0956792518000074 Published online by Cambridge University Press

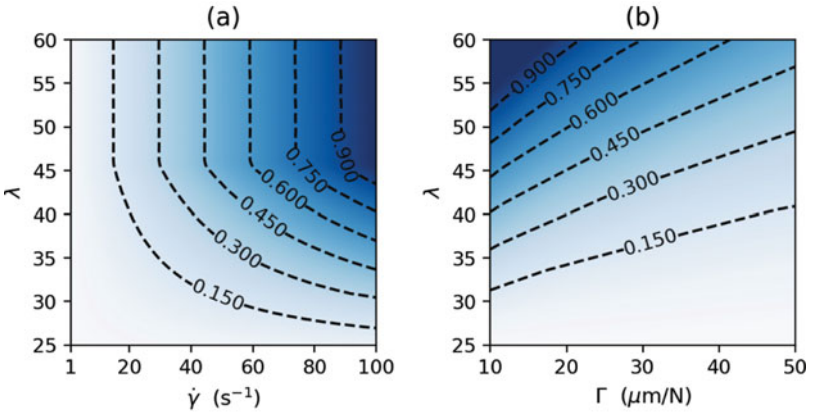

FIGURE 7. Maximum normalised fragmentation force experienced by a sample ellipsoid as a function of the shear rate $\dot{\gamma}$ and the viscosity ratio λ (a) and the interfacial tension Γ and the viscosity ratio (b). In (a), $\Gamma = 40 \times 10^{-6}$ N/m, and in (b) $\dot{\gamma} = 10$ m/s.

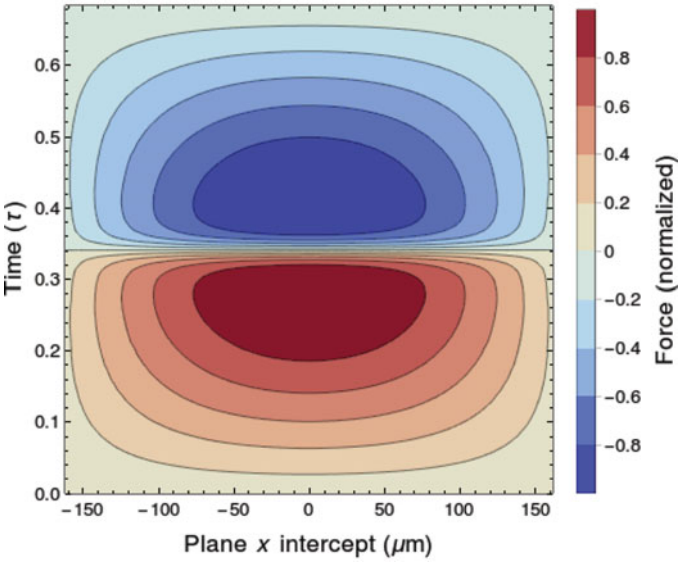

FIGURE 8. Normalised fragmentation force with respect to a plane normal to $(1, 0, 0)$ and intersecting a sample ellipsoid at $\mathbf{x} = (x, 0, 0)$ (horizontal axis) over time (vertical axis). $\mathbf{a}_0 = (180, 140, 100)$ μm.

x-axis to the midpoint, the fragmentation force increases, and then decreases again as the plane moves from the centre to the other end; again due to the symmetries of the system.

3.3 Aggregate fragmentation

Figure 9 shows the results of exhaustive fragmentation on the initial set of 39 aggregates for each of the three fragmentation methods. Each subplot shows a two-dimensional histogram of the normalised frequency of fragmentations, in which the horizontal axis corresponds to the size of the parent aggregate, and the vertical axis to the ratio of the

https://doi.org/10.1017/S0956792518000074 Published online by Cambridge University Press

size of a daughter aggregate to its parent. Because, a fragmentation of an aggregate of size m into a daughter of size k also necessarily gives rise to a daughter of size $m - k$, the plots are symmetric about the horizontal line $r = 0.5$. The probabilities are normalised by parent size, so that the entry corresponding to $x = m$ on the horizontal axis and $r = k$ on the vertical axis indicates the probability that an aggregate of size m fragments into daughters of size k and $m - k$, given that the parent is of size m and fragments.

Figure 9(a) shows the results for the *first edge* fragmentation method. Recall that this method computes the fragmentation force for each edge, in order of length, over the entire period of motion before proceeding to the next edge. As the parent size increases, erosion quickly becomes the dominant fragmentation mechanism. This can be seen by the larger probabilities along the vertical boundaries of the plot: parents fragment into one small and one large daughter. This is the same pattern we observed in our original work on this problem, in which we used the first edge method and treated the aggregates as non-deformable solids [6].

Figure 9(b) shows the results for the *first time* fragmentation method, in which the fragmentation force is computed at each time point for each edge before moving on to the next longest edge. We still observe a tendency towards erosion as parent size increases, but it is less dominant than in the first edge method, which is to say that we observe an increase in the frequency of fragmentations into more evenly-sized daughters. Finally, Figure 9(c) shows the post-fragmentation density function for the *global maximum* method, which computes the fragmentation force at all times for all edges and chooses the largest one. This method shows a significant shift towards splitting in comparison to the other two methods, although erosion often still dominates.

We can make sense of these results as follows. The bacterial centres of mass tend be clustered in a central area, so that the density of these points decreases with distance from the origin. A MST taken on such a such a set of points is likely to have its longest edges towards the periphery of the aggregate. These edges are in turn more likely to connect singletons or smaller aggregates to the parent aggregate, as opposed to more central, shorter edges, which will tend to separate the tree into two more evenly sized subtrees. An example of this can be observed in Figure 4: the relatively short highlighted edge splits the tree into two subtrees of comparable size (red and blue centres of mass) and is buried near the centre of the aggregate.

4 Conclusions and future plans

We have presented a method to check for fragmentation in free-floating aggregates in simple shear flow, which combines a model for the forces on the surface an ellipsoid with one for the deformation of an ellipsoid in flow. We then used this method in a simulation of exhaustive fragmentation on an initial dataset based on images of 39 microbial aggregates. We compared three different methods for checking for fragmentation, one which we have used previously in a simpler fragmentation simulation. The post-fragmentation density functions we obtain for each method are different than the normal and log-normal distributions, which are widespread in the literature. In particular, the functions exhibit a range of behaviours from almost pure erosion in the case of the first edge method to an erosion/splitting mix in the case of the global maximum method. Even in the latter case,

https://doi.org/10.1017/S0956792518000074 Published online by Cambridge University Press

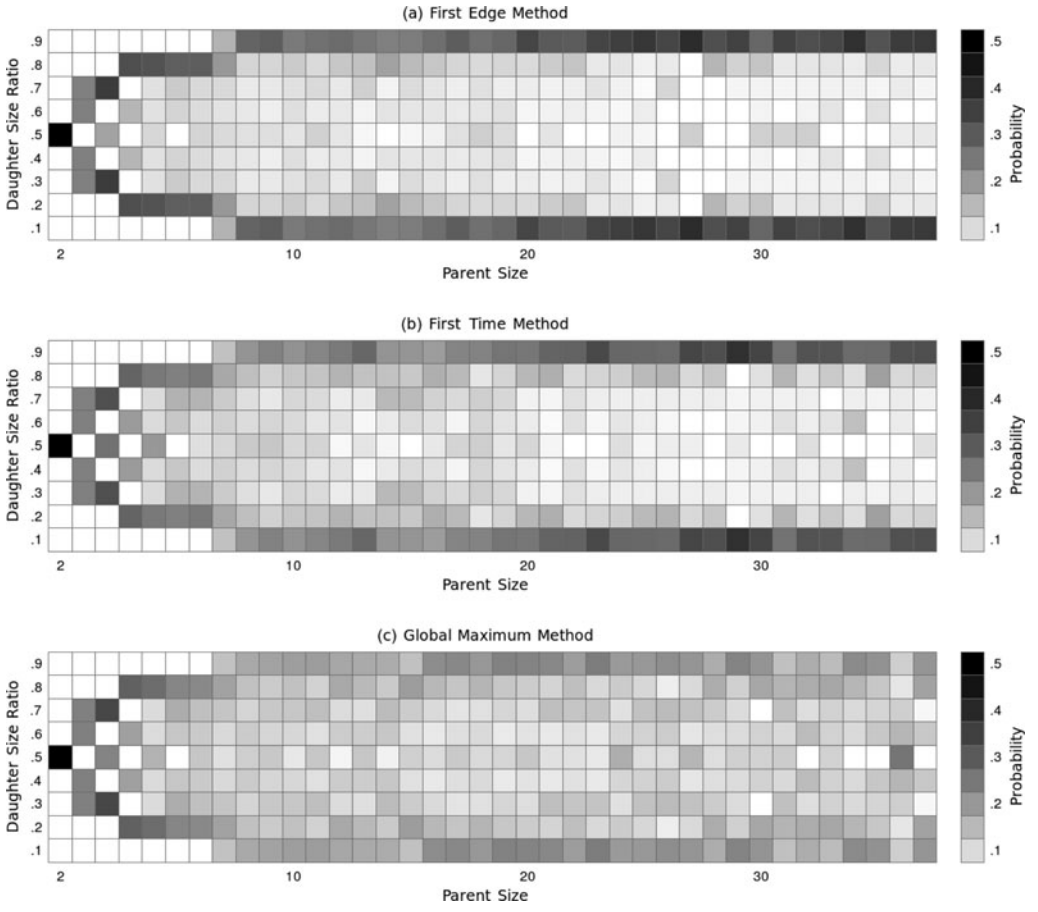

FIGURE 9. Post-fragmentation density functions for (a) the *first edge* method, (b) the *first time* method, and (c) the *global maximum* method. The horizontal axis corresponds to the size of the fragmenting aggregate, and the vertical axis to the ratio of daughter size to mother size.

erosion remains an important fragmentation mechanism. These results can inform the choice of fragmentation kernels in population-balance models, primarily by suggesting a more important role for erosion than is generally assumed.

With this hybrid methodology, we are now ready to proceed with upscaling these results to a population level model as well as comparing the predictions with experimental size-structured population data.

Acknowledgements

We would like to thank Charles Tucker III, Eric Wetzel, and Nancy Jackson for making their code available to us and for helpful discussions on the behaviour of their model, and Dr. John Younger for helpful discussions on an application of this work to microbial flocculation.

References

[1] Blaser, S. (2000) Break-up of flocs in contraction and swirling flows. *Colloids Surf. Physicochem. Eng. Asp.* **166**(1–3), 215–223.

[2] Blaser, S. (2000) Flocs in shear and strain flows. *J. Colloid Interface Sci.* **225**(2), 273–284.

[3] Blaser, S. (2002) Forces on the surface of small ellipsoidal particles immersed in a linear flow field. *Chem. Eng. Sci.* **57**(3), 515–526.

[4] Bortz, D. M., Jackson, T. L., Taylor, K. A., Thompson, A. P. & Younger, J. G. (2008) Klebsiella pneumoniae flocculation dynamics. *Bull. Math. Biol.* **70**(3), 745–768.

[5] Bratby, J. (2008) *Coagulation and Flocculation in Water and Wastewater Treatment*, 2nd ed., International Water Association, Seattle, WA.

[6] Byrne, E., Dzul, S., Solomon, M., Younger, J. & Bortz, D. M. (2011) Postfragmentation density function for bacterial aggregates in laminar flow. *Phys. Rev. E* **83**(4), 041911.

[7] Gaboriaud, F., Gee, M. L., Strugnell, R. & Duval, J. F. L. (2008) Coupled electrostatic, hydrodynamic, and mechanical properties of acterial interfaces in aqueous media. *Langmuir* **24**(19), 10988–10995.

[8] Hammond, J. F., Stewart, E., Younger, J. G., Solomon, M. J. & Bortz, D. M. (2014) Variable viscosity and density biofilm simulations using an immersed boundary method, Part I: Numerical scheme and convergence results. *Comput. Model. Eng. Sci.* **98**(3), 295–340.

[9] Jackson, N. E. & Tucker III, C. L. (2003) A model for large deformation of an ellipsoidal droplet with interfacial tension. *J. Rheol.* **47**(3), 659–682.

[10] James, D., Yogachandran, N., Loewen, M., Liu, H. & Davis, A. (2003) Floc rupture in extensional flow. *J. Pulp Pap. Sci.* **29**(11), 377–383.

[11] Kléman, M. & Lavrentovich, O. D. (2003) *Soft Matter Physics: An Introduction*, Springer, New York.

[12] Kobayashi, M. (2004) Breakup and strength of polystyrene latex flocs subjected to a converging flow. *Colloids Surf. Physicochem. Eng. Asp.* **235**(1–3), 73–78.

[13] Kobayashi, M. (2005) Strength of natural soil flocs. *Water Res.* **39**(14), 3273–3278.

[14] Liss, S. N., Droppo, I. G., Leppard, G. G. & Milligan, T. G. (editors) (2007) *Flocculation in Natural and Engineered Environmental Systems*, CRC Press, Boca Raton, FL.

[15] Mirzaev, I. & Bortz, D. M. (2015) Criteria for linearized stability for a size-structured population model. arXiv : 1502.02754.

[16] Mirzaev, I. & Bortz, D. M. (2017) A numerical framework for computing steady states of structured population models and their stability. *Math. Biosci. Eng.* **14**(4), 933–952.

[17] Mirzaev, I., Byrne, E. C. & Bortz, D. M. (2016) An inverse problem for a class of conditional probability measure-dependent evolution equations. *Inverse Probl.* **32**(9), 095005.

[18] Nopens, I. (2005) *Modelling the Activated Sludge Flocculation Process: A Population Balance Approach*. PhD, Universiteit Gent.

[19] Rueb, C. J. & Zukoski, C. F. (1997) Viscoelastic properties of colloidal gels. *J. Rheol.* **41**(2), 197–218.

[20] Solsvik, J., Tangen, S. & Jakobsen, H. A. (2013) On the constitutive equations for fluid particle breakage. *Rev Chem. Eng.* **29**(5), 241–356.

[21] Stotsky, J. A., Hammond, J. F., Pavlovsky, L. Stewart, E. J., Younger, J. G., Solomon, M. J. & Bortz, D. M. (2016) Variable viscosity and density biofilm simulations using an immersed boundary method, Part II: Experimental validation and the heterogeneous rheology-IBM. *J. Comput. Phys.* **316**, 204–222.

[22] Wetzel, E. D. & Tucker III, C. L. (2001) Droplet deformation in dispersions with unequal viscosities and zero interfacial tension. *J. Fluid Mech.* **426**, 199–228.

[23] Yarin, A., Gottlieb, O. & Roisman, I. (1997) Chaotic rotation of triaxial ellipsoids in simple shear flow. *J. Fluid Mech.* **340**, 83–100.